

Original Investigation

Generalized Linear Binning to Compare Hyperpolarized ^{129}Xe Ventilation Maps Derived from 3D Radial Gas Exchange Versus Dedicated Multislice Gradient Echo MRI

Mu He, PhD, Ziyi Wang, MS, Leith Rankine, MS, Sheng Luo, PhD, John Noulds, PhD, Rohan Virgincar, PhD, Joseph Mammarappallil, MD, PhD, Bastiaan Driehuys, PhD

Rationale: Hyperpolarized ^{129}Xe ventilation MRI is typically acquired using multislice fast gradient recalled echo (GRE), but interleaved 3D radial ^{129}Xe gas transfer MRI now provides dissolved-phase and ventilation images from a single breath. To investigate whether these ventilation images provide equivalent quantitative metrics, we introduce generalized linear binning analysis.

Methods: This study included 36 patients who had undergone both multislice GRE ventilation and 3D radial gas exchange imaging. Images were then quantified by linear binning to classify voxels into one of four clusters: ventilation defect percentage (VDP), Low-, Medium- or High-ventilation percentage (LVP, MVP, HVP). For 3D radial images, linear binning thresholds were generalized using a Box-Cox rescaled reference histogram. We compared the cluster populations from the two ventilation acquisitions both numerically and spatially.

Results: Interacquisition Bland-Altman limits of agreement for the clusters between 3D radial vs GRE were (-7% to 5%) for VDP, (-10% to 14%) for LVP, and (-8% to 8%) for HVP. While binning maps were qualitatively similar between acquisitions, their spatial overlap was modest for VDP (Dice = 0.5 ± 0.2), and relatively poor for LVP (0.3 ± 0.1) and HVP (0.2 ± 0.1).

Conclusion: Both acquisitions yield reasonably concordant VDP and qualitatively similar maps. However, poor regional agreement (Dice) suggests that the two acquisitions cannot yet be used interchangeably. However, further improvements in 3D radial resolution and reconciliation of bias field correction may well obviate the need for a dedicated ventilation scan in many cases.

Key Words: Hyperpolarized ^{129}Xe MRI; Multislice GRE; 3D Radial; Acquisition; Quantification.

© 2019 The Association of University Radiologists. Published by Elsevier Inc. All rights reserved.

INTRODUCTION

Hyperpolarized ^{129}Xe MRI enables rapid, noninvasive imaging of both pulmonary ventilation (1–3) and gas-exchange (4–6). Such functional images can be quantitatively analyzed to provide a means of visualizing regional disease, its progression, and therapy response. ^{129}Xe ventilation MRI has been applied to conditions, such as chronic obstructive pulmonary disease (COPD) (7), asthma (3), and cystic fibrosis (8,9), which typically exhibit elevated ventilation defect percentage (VDP). To date, the majority of hyperpolarized gas MR ventilation acquisitions have employed multislice fast gradient recalled echo (GRE) imaging (2,10,11). Such sequences are fast, robust, readily implemented on most scanner platforms, and reconstruct in

Acad Radiol 2019; ■:1–11

From the Department of Electrical and Computer Engineering, Duke University, Durham, North Carolina (M.H.); Center for In Vivo Microscopy, Duke University Medical Center, Box 3302, Durham, NC 27710 (M.H., Z.W., L.R., J.N., R.V., B.D.); Department of Biomedical Engineering, Duke University, Durham, North Carolina (Z.W., R.V., B.D.); Medical Physics Graduate Program, Duke University Medical Center, Durham, North Carolina (L.R., B.D.); Department of Biostatistics & Bioinformatics, Duke University Medical Center, Durham, North Carolina (S.L.); Department of Radiology, Duke University Medical Center, Durham, North Carolina (J.N., J.M., B.D.). Received June 23, 2019; revised October 2, 2019; accepted October 16, 2019. Address correspondence to: B.D. e-mail: bastiaan.driehuys@duke.edu

© 2019 The Association of University Radiologists. Published by Elsevier Inc. All rights reserved.

<https://doi.org/10.1016/j.acra.2019.10.016>

real-time. The resulting images can be analyzed quantitatively through rescaling of the intensity histogram followed by linear binning to both spatially resolve and quantify VDP, as well as other intensity clusters (12). However, alternative ventilation acquisitions have emerged, featuring either higher speed, such as spiral (13), or more efficient use of magnetization, such as 3D balanced steady-state free precession (14). Beyond sequences dedicated to ventilation, ¹²⁹Xe gas exchange MRI using 3D radial trajectories, while primarily developed to image gas uptake into the interstitial barrier tissues and its transfer into the red blood cells, also produces an isotropic ventilation image.

Because the ventilation intensity distribution from MRI lacks an absolute scale, it must be rescaled in order to apply intensity thresholds that can parse the data into different functional levels. To date, the most commonly used ventilation MRI strategy has employed a multislice GRE scans, acquired coronally, in the anterior to posterior direction. When such scans are acquired in healthy subjects, the underlying intensity histogram, after being rescaled by the top percentile of intensities, exhibits a nearly perfect Gaussian shape. This observation led naturally to our published approach that sets the binning thresholds based on the mean and standard deviation of the rescaled intensity distribution derived from a healthy reference population (2). However, it has since come to light from our work and others that images acquired using different sequences, slice orders, acquisition planes, or using 3D encoding, result in rescaled reference distributions that are typically not perfectly Gaussian (4). Thus, for such acquisitions, it is necessary to develop a more generalized approach to determining binning thresholds.

Secondly, the ability to now obtain an isotropic ventilation image as part of the gas exchange acquisition, raises the practical question as to whether and when this level of ventilation imaging detail is sufficient. Compared to multislice GRE acquisition, which samples *k*-space in a Cartesian fashion, 3D radial images are acquired with very short echo time (TE), which may reduce susceptibility artifacts near the ribs. Moreover, 3D acquisitions can better capture the gravitationally and other physiological-related intensity gradients because the entire volume is sampled throughout the breath-hold and can be reconstructed in arbitrary keys of data (15). Despite these merits, the 3D radial images acquired as part of the gas exchange MRI are significantly undersampled and are typically reconstructed with lower in-plane resolution than multislice 2D acquisitions.

Thus, in this work, we sought to address the degree to which 3D radial ventilation images acquired as part of a gas exchange study could deliver similar quantitative results compared to standard multislice GRE acquisition. We used our established linear-binning method (2,4,16) to derive the quantitative metrics—VDP, low-, medium- and high-ventilation percentage (LVP, MVP, and HVP, respectively). In order to manage the non-Gaussian reference distributions derived from the 3D radial acquisition we provide a generalized method to set binning thresholds. We then evaluate the

degree to which the quantitative metrics derived from the two acquisitions agreed both globally and regionally. The results of this investigation may help answer the question of whether and to what degree ventilation images derived from radially acquired ¹²⁹Xe gas exchange can substitute for a dedicated multislice GRE acquisition.

METHODS

Subject Inclusion and Exclusion Criteria

A total of 36 cases were included from subjects who had undergone both multislice GRE MRI and 3D radial gas exchange MRI, each with ventilation image signal-to-noise ratio (SNR) greater than 6. This cohort included eleven COPD (age: 62.5 ± 12.2 years, FEV1%: 50.1 ± 22.0), three left heart failure (age: 65.4 ± 6.5 years, FEV1%: 70.6 ± 17.2), five pulmonary artery hypertension (age: 51.2 ± 6.9 years, FEV1: 71.0 ± 12.9), six chronic thromboembolic pulmonary hypertension (age: 48.3 ± 18.1 years, FEV1: 77.5 ± 13.6), and 11 nonspecific interstitial pneumonia (age: 55.2 ± 10.2 years, FEV1: 58.4 ± 10.6) subjects. All subjects provided written informed consent prior to the scan. Studies were conducted under a protocol approved by the Institutional Review Board, and subject to an FDA Investigational New Drug Application #109,490.

¹²⁹Xe Polarization and Delivery

Isotopically enriched ¹²⁹Xe (86%) in volumes of 250–500 mL (GRE) or 700 mL (3D radial) was polarized by rubidium-vapor spin-exchange optical pumping (17) using a commercially available polarizer (Model 9810, Polarean, Inc., Durham, NC). After polarization, ¹²⁹Xe was cryogenically accumulated and thawed into a Tedlar bag. The dose was then supplemented with ultra-high-purity Nitrogen gas to fill the bag to its full 1 L volume and stored in the 20 Gauss holding field of a polarization measurement station (Model 2881, Polarean, Inc., Durham, NC). This also enabled measurement of the ¹²⁹Xe dose acitivity immediately prior to its delivery to the patient. The dose equivalents were 97 ± 13 mL for GRE and 187 ± 15 mL for 3D radial (18).

MR Image Acquisition

All MR scans were acquired on a 3-Tesla SIEMENS MAGNETOM Trio scanner (VB19). Briefly, subjects were scanned in the supine position with a flexible quadrature ¹²⁹Xe vest coil (Clinical MR Solutions, Brookfield, WI) that was tuned to the 34.09 MHz ¹²⁹Xe frequency and proton-blocked to permit acquiring anatomical scans using the ¹H body coil. After the initial localizers and proton thoracic cavity scans (described in the following), subjects underwent a dedicated ventilation MRI using a fast, spoiled gradient echo sequence (GRE) sequence, followed by a 3D radial gas exchange MRI. Scans were performed in the supine position

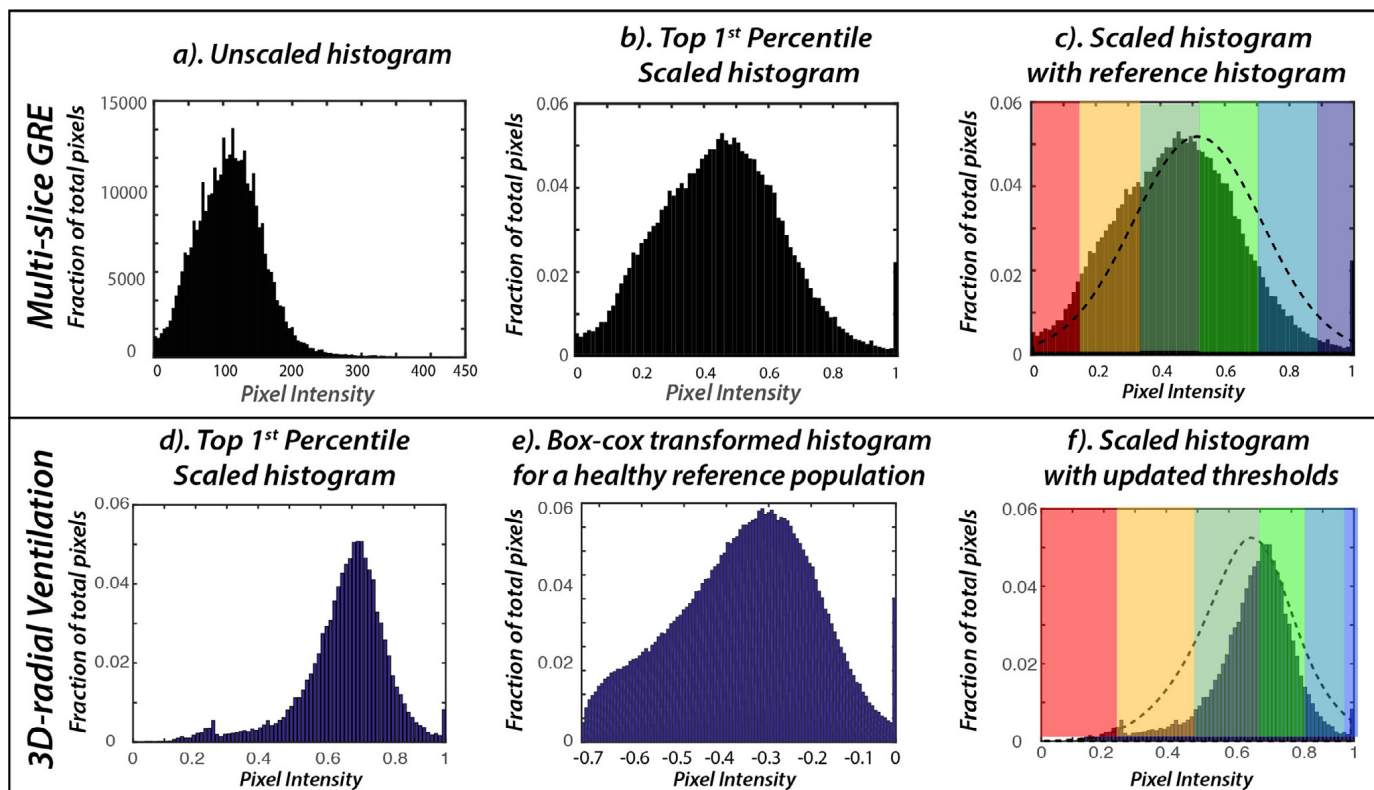


Figure 1. Setting binning thresholds for a Gaussian vs non-Gaussian healthy reference population. (a) unscaled histogram for a healthy subject acquired using multislice GRE sequence. (b) This histogram was rescaled by the top one percentile of intensities (c) then binned based on thresholds derived from a Gaussian reference distribution. (d) For 3D radial acquisitions, the histogram for a healthy subject is skewed. (e) Thus, the average healthy reference histogram first underwent a Box-Cox transformation to render it into a normal one distribution. (f) From this, the mean and standard deviation were derived and used to determine binning thresholds . These were transformed back to the original distribution, and were nonlinearly spaced at (0.227, 0.477, 0.686, 0.828, 0.940); however each bin encompasses the same percentage of the histogram as its Gaussian counterpart.

and subjects were coached to inhale the gas doses from functional residual capacity.

GRE ventilation images were acquired with field of view (FOV) = 38.4 × 36 cm, matrix = 96 × 90, slice thickness = 12–18 mm, bandwidth = 170 Hz/pixel, flip angle = 10°, repetition time (TR)/TE = 7.65/3 milliseconds, and resolution = 4 × 4 × slice thickness (mm³). A matching image of the thoracic cavity was acquired using the ¹H body coil with the subject positioned in the ¹²⁹Xe coil and inhaling 1 L of room air from a bag to match lung inflation. The ¹H scan employed a steady state fast spin echo sequence (SSFSE) with FOV = 38.4 cm, matrix = 192 × 192, slice thickness = 12–18 mm, echo spacing = 3.46 milliseconds, TR/TE = 800/31 milliseconds, NEX = 0.5 (half Fourier), bandwidth = 789 Hz/pixel, flip angle = 108°, and resolution = 2 × 2 × slice thickness (mm³).

Subsequently, 3D radial ventilation images were acquired as part of the gas exchange acquisition (19). The gas and dissolved-phase ¹²⁹Xe distributions were each encoded using 1000 randomized radial views and reconstructed to 128³ matrix using an isotropic FOV (36–40 cm)³ (20, 21), TE/TR = TE₉₀/7.5 milliseconds, TE₉₀ = 0.45–0.5 milliseconds, bandwidth = 800 Hz/pixel (dwell time = 9.8 us) and flip angles = ~0.5/20°. This was accompanied by a matching 3D radial ¹H thoracic cavity scan for which subjects again inhaled

1 L room air. This acquisition consisted of 4601 radial views, 64 samples per projection, TE/TR = 0.52/3.54 milliseconds, readout bandwidth = 562 Hz/pixel, flip angle = 5°.

Image Analysis

Linear Binning Quantification for Non-Gaussian Ventilation Distributions

Both the multislice GRE and isotropic 3D radial ventilation images were quantified using the previously described linear binning method (2,4). The GRE ventilation images were parsed into individual bins using the published thresholds that had been established based on a healthy reference cohort scanned at 1.5 Tesla (2,16). The process of rescaling by the top percentile and binning of the GRE scan is illustrated in (Fig. 1a-c). Note that both the individual data from this subject and the healthy reference population appear Gaussian upon visual examination. By contrast, the 3D radial acquisition, after bias field correction and top percentile rescaling, generates a skewed-shifted signal distribution in the healthy volunteer (Fig 1d), which is also observed in the broader healthy cohort (Fig 1e). Thus, in order to derive appropriate binning thresholds, a Box-Cox transform was applied to render the skewed healthy reference distribution γ into a normal one $\gamma(\lambda)$ using a transformation parameter $\lambda = 1.348$.

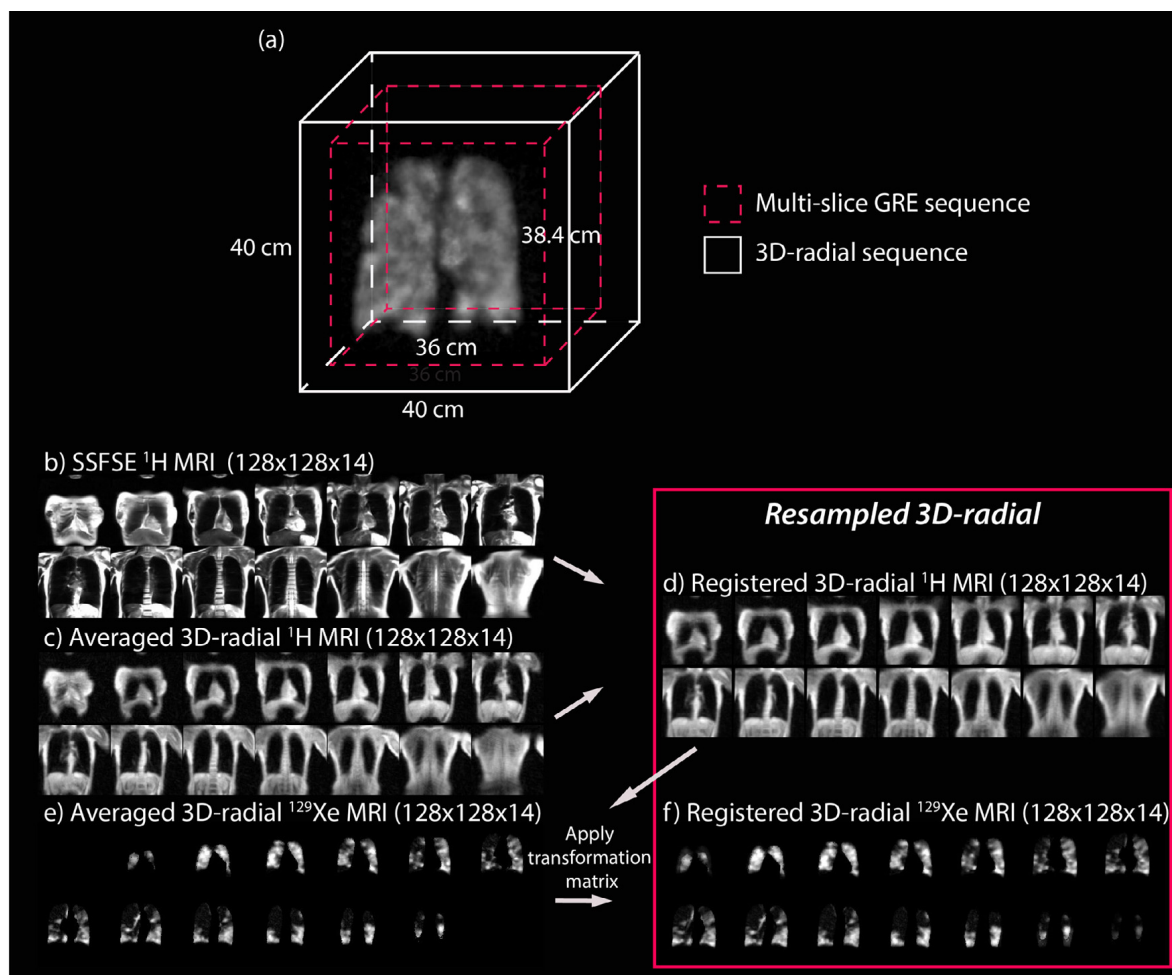


Figure 2. Resampling and registration workflow for pixel-by-pixel comparison of GRE and 3D radial derived maps. (a) The z-dimension of the 3D radial images was first cropped to match the slice coverage of the multislice GRE acquisition. (c, e) cropped 3D radial images were then interpolated to $128 \times 128 \times 14$. The (c) interpolated 3D radial 1H images were registered to (b) the SSFSE 1H images using a SyN diffeomorphic registration with rigid and affine as preregistration steps. This registration yielded the (d) registered 3D radial 1H images. The associated transformation matrix was applied to the (e) averaged 3D radial ^{129}Xe images to register them to the GRE space. GRE, gradient recalled echo; SSFSE, steady state fast spin echo sequence.

$$\gamma(\lambda) = \begin{cases} \frac{\lambda^2 - 1}{\lambda}, & \text{if } \lambda \neq 0 \\ \log y, & \text{if } \lambda = 0 \end{cases} \quad (1)$$

After transformation the healthy cohort distribution was characterized by mean of -0.36 and a standard deviation (SD) of 0.16, which were used to generate binning thresholds in the transformed space. These threshold values were then transformed back to the original distribution space using [Equation 2](#):

$$y = \sqrt[\lambda]{\lambda \cdot \gamma(\lambda) + 1} \quad (2)$$

Note that this generalized approach creates thresholds that are no longer evenly spaced, but the resulting bins still encompass the same percentages of voxels as for the case of the purely Gaussian distributions (34.1% for the bins within 1 SD of the mean, 13.6% for the next bin). The resulting thresholds for the 3D acquisition were 0.227, 0.477, 0.686,

0.828, and 0.940 ([Fig 1f](#)). These were used to determine VDP, as well as LVP, MVP, HVP for the 3D acquisitions, while the GRE scans were quantified using the previously reported of 0.16, 0.34, 0.52, 0.7, and 0.88.

Resampling and Registration for Pixel-wise Comparison of GRE vs 3D radial-derived maps

To compare the spatial overlap of the metrics from the two acquisitions, the 3D radial images were resampled to a $128 \times 128 \times 14$ matrix with $\text{FOV} = 38.4 \text{ cm}$ and coregistered to the multislice GRE images, as illustrated in [Figure 2](#). The multislice GRE images were acquired as a $96 \times 90 \times 14$ matrix with a native resolution of $4 \times 4 \times 15 \text{ mm}$, whereas the 3D radial images were reconstructed as a $128 \times 128 \times 128$ matrix, with a nominal voxel size of 2.8^3 or 3.1^3 mm^3 . The multislice GRE with a $\text{FOV} = 38.4 \times 36 \text{ cm}$ was first zero-filled to $96 \times 96 \times 14$ and then interpolated to $128 \times 128 \times 14$. Similarly, the SSFSE proton images, acquired at a native resolution of $192 \times 192 \times 14$ were down

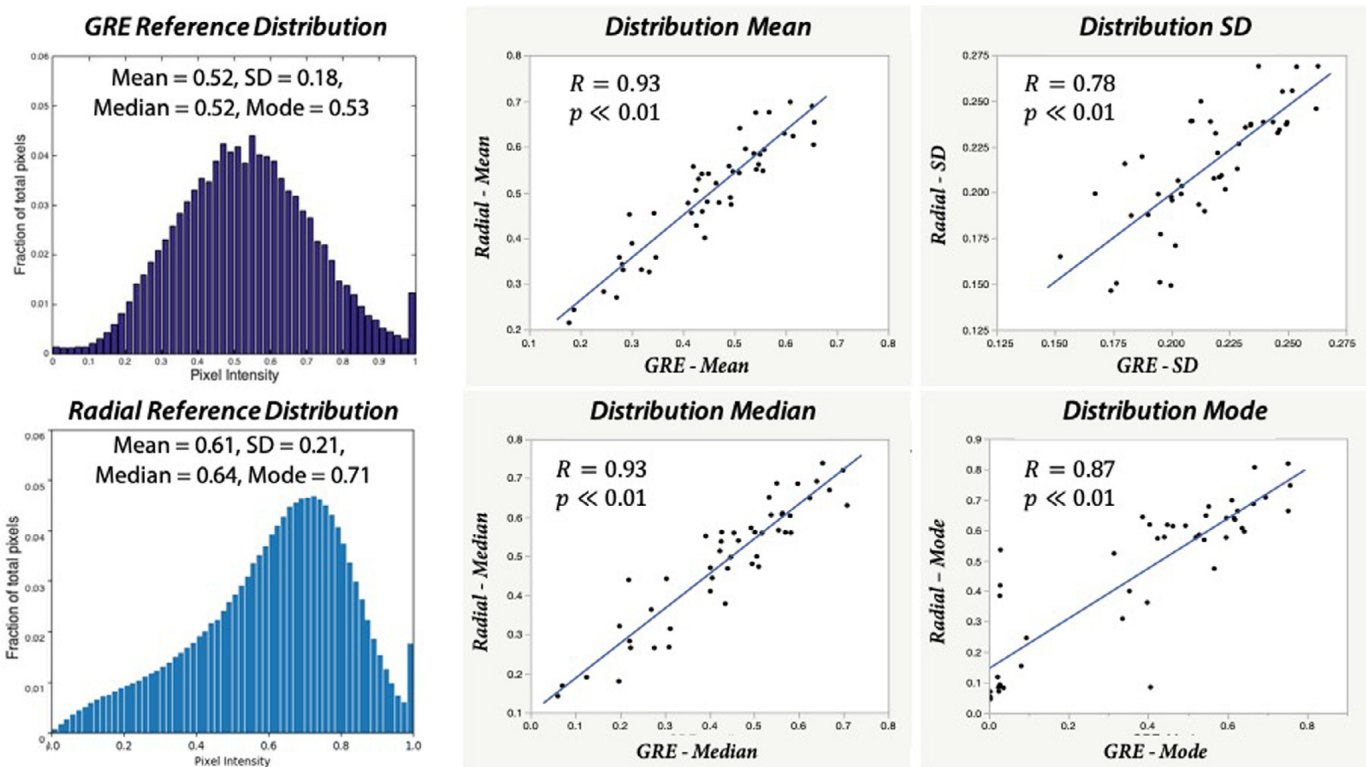


Figure 3. Comparison of the multislice GRE and 3D radial top-percentile-scaled healthy reference distributions, and the correlation of the distribution parameters across all patients examined. While the rescaled GRE distribution is Gaussian in appearance, the radial distribution is skewed, with a significantly higher mean, median, mode, and standard deviation. However, these distribution parameters correlated strongly between the two acquisitions across the entire cohort. GRE, gradient recalled echo.

sampled to $128 \times 128 \times 14$. The 3D radial ventilation images were first zero-filled ($\text{FOV} = 36 \text{ cm}$) or cropped ($\text{FOV} = 40 \text{ cm}$) to fit into the 38.4^3 cm^3 FOV and then interpolated to 128^3 . Subsequently, the portions of their z-dimension that were not covered by the corresponding GRE acquisition were removed. Next, cropped 3D radial images were down-sampled to $128 \times 128 \times 14$. Subsequently, the resampled proton 3D radial images were registered to the proton SSFSE images ($128 \times 128 \times 14$) using a rigid, affine, and symmetric normalization diffeomorphic registration packages from the Advanced Normalization Tools (ANTS) toolkit (22) that was constrained to occur only within the proton image masks. The resulting transformation matrix was applied to the resampled ^{129}Xe 3D radial ventilation images to register them to the same space as the corresponding ^{129}Xe GRE images.

Statistical Analysis

To test the degree of concordance between the metrics VDP, LVP, MVP, and HVP derived from the two acquisitions, Bland-Altman plots were used to determine any bias and establish the limits of agreement. These metrics were also evaluated by their correlation coefficients. To further compare the distributions without introducing quantization errors associated with discrete binning, we also calculated the correlation of the underlying GRE and radial distribution parameters. Finally, the spatial similarities for VDP, LVP, MVP, and

HVP were compared between the two acquisitions using the Dice coefficient. All statistical analyses were performed using JMP 11 (SAS Institute Inc., Cary, NC).

RESULTS

Inter-Method Comparison of Distribution Parameters

Figure 3 compares the rescaled healthy cohort reference distributions derived from the GRE vs radial acquisitions. While the GRE distribution is well represented by a Gaussian function, the 3D radial distribution is skewed towards higher values, with a higher mean, median, mode, and SD. Figure 3, also shows the correlation between these distribution parameters for the GRE and radial acquisitions for each patient in the cohort. These plots confirm that while the distribution shapes may be different, their distribution parameters correlate strongly between the acquisitions.

Inter-Method Comparison of Binning Percentages

Global Comparison

Representative scans and associated maps for 3D radial vs multislice GRE acquisitions acquired from a COPD patient are shown in Figure 4. In this patient with obvious ventilation abnormalities, the images and maps exhibit good qualitative agreement between the two acquisitions. This was reflected in quantitative metrics that also agreed well, with VDP of

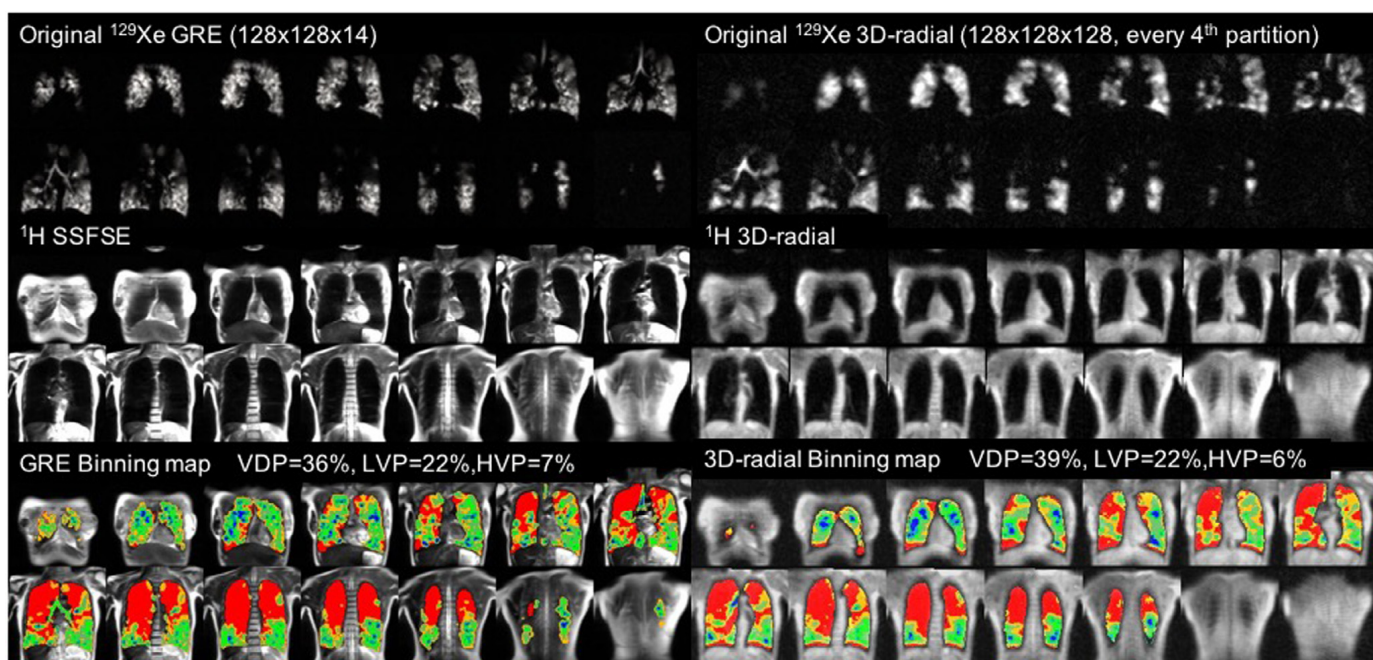


Figure 4. Comparison of the multislice GRE and 3D radial images and quantitative metrics VDP, LVP, and HVP in a COPD patient. Note, the 3D radial images are reconstructed with 128 partitions, and only every fourth one is shown here. COPD, chronic obstructive pulmonary disease; GRE, gradient recalled echo; HVP, high-ventilation percentage; LVP, low-ventilation percentage; VDP, ventilation defect percentage.

36% vs 39%, identical LVP of 22%, and HVP of 7% vs 6%. When examined by disease group, the ventilation defects were considerably higher for COPD relative to the other groups **Table 1**. The correlation coefficient (r) for the entire cohort was 0.99 for VDP, 0.74 for LVP, and 0.83 for HVP.

The Bland-Altman plot for the key quantitative metrics derived from radial vs GRE acquisitions is shown in **Figure 5**. The limits of agreement for 3D radial vs GRE for VDP were (-5% to 7%), for LVP were (-14% to 10%), and for HVP were (-8% to 8%). The biases were small and insignificant

between the two acquisitions, with a 1.6% bias for VDP ($p < 0.01$), -1.8% for LVP ($p = 0.06$), and -0.1% for HVP ($p = 0.84$).

Pixel-By-Pixel Comparison of Binning Maps

The effect of resampling the 3D radial images to the multi-slice GRE space is illustrated in **Figure 6**. The left side of the figure shows every 5th partition of the original data set and its associated maps, while the right side shows the resampled and

TABLE 1. Global Comparison of Quantitative Metrics Derived from GRE and 3D Radial Acquisitions

Statistic	COPD ($n = 11$)	LHF ($n = 3$)	PAH ($n = 5$)	CTEPH ($n = 6$)	NSIP ($n = 11$)	Total ($n = 36$)
<i>Multislice GRE acquisition</i>						
VDP (%)	35.2 ± 19.4	12.3 ± 7.9	9.6 ± 6.8	8.7 ± 5.6	4.6 ± 2.8	16.7 ± 17.7
LVP (%)	25.1 ± 6.9	21.8 ± 9.5	19.5 ± 6.0	17.8 ± 8.8	16.7 ± 4.8	20.4 ± 7.6
HVP (%)	6.2 ± 1.8	10.5 ± 5.1	8.5 ± 3.9	11.7 ± 5.7	13.8 ± 7.4	10.1 ± 5.9
<i>3D radial acquisition</i>						
VDP (%)	33.0 ± 19.9	10.8 ± 5.2	9.2 ± 7.3	7.1 ± 4.7	3.2 ± 2.1	15.1 ± 17.4
LVP (%)	26.7 ± 4.9	24.0 ± 7.6	23.2 ± 9.7	23.0 ± 11.0	15.6 ± 7.1	22.3 ± 8.6
HVP (%)	6.6 ± 2.8	11.5 ± 4.7	9.9 ± 3.2	10.3 ± 3.9	13.9 ± 8.8	10.1 ± 6.1
<i>Differences between GRE vs 3D radial acquisitions</i>						
Δ VDP (%)	2.2 ± 3.2	0.7 ± 2.0	0.4 ± 3.1	1.9 ± 3.2	1.4 ± 1.8	1.6 ± 2.6
Δ LVP (%)	1.7 ± 5.2	2.2 ± 4.6	3.7 ± 6.6	5.2 ± 5.3	1.1 ± 5.8	-1.8 ± 5.8
Δ HVP (%)	0.5 ± 2.0	1.0 ± 3.6	1.3 ± 3.1	1.4 ± 4.8	0.0 ± 4.0	-0.1 ± 3.5
<i>Correlation coefficient (r)</i>						
VDP	0.99	0.99	0.91	0.90	0.76	0.99
LVP	0.67	0.88	0.47	0.88	0.58	0.74
HVP	0.68	0.73	0.62	0.56	0.89	0.83

COPD, chronic obstructive pulmonary disease; CTEPH, chronic thromboembolic pulmonary hypertension; HVP, high-ventilation percentage; LHF, left heart failure; LVP, low-ventilation percentage; NSIP, nonspecific interstitial pneumonia; PAH, pulmonary artery hypertension; VDP, ventilation defect percentage.

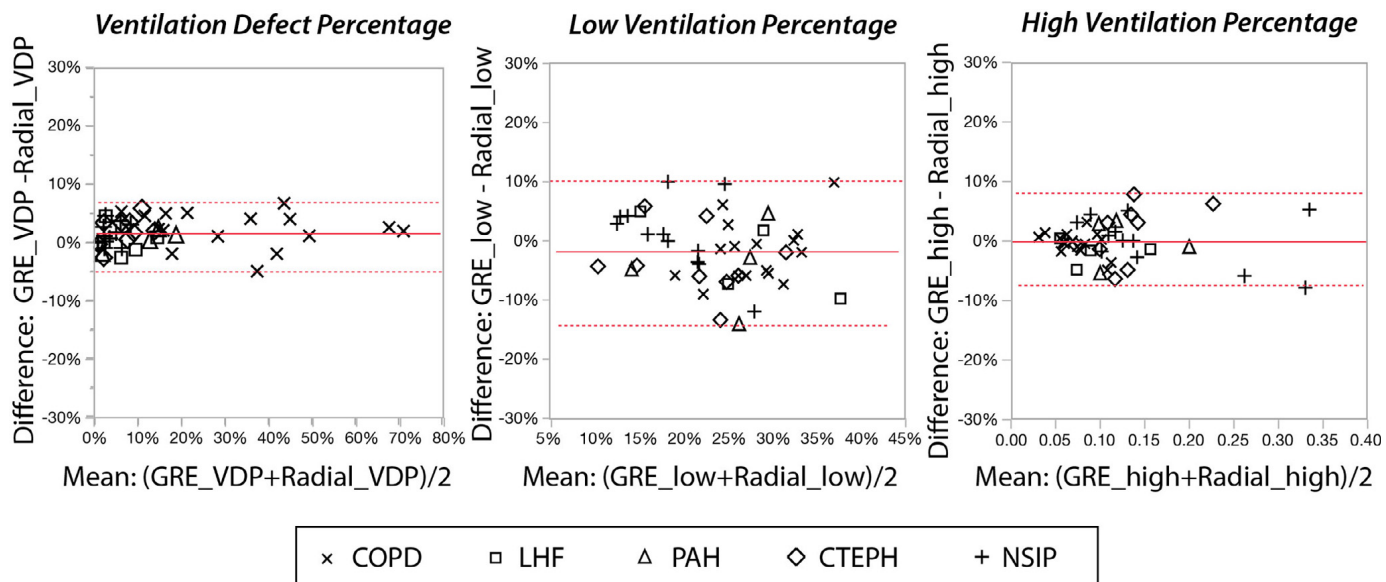


Figure 5. The limits of agreement between radial and GRE acquisitions for VDP were (−5% to 7%) with a 1.6% bias, for LVP were (−14% to 10%) with a −1.8% bias, and for HVP were (−8% to 8%) with a −0.1% bias. GRE, gradient recalled echo; HVP, high-ventilation percentage; LVP, low-ventilation percentage; VDP, ventilation defect percentage.

rescaled data in the GRE space. This COPD subject exhibits substantial ventilation defects as well as a low-ventilation region in the upper right lobe on the 10th slice (arrow), and this same pattern can be seen in the resampled data. In aggregate, resampling of the 3D radial images left the quantitative metrics largely unchanged, with average changes of $\Delta\text{VDP} = 1.4 \pm 4.2\%$, $\Delta\text{LVP} = 0.2 \pm 5.8\%$, and $\Delta\text{HVP} = 3.6 \pm 2.5\%$.

Figure 7 shows the qualitative comparison of the rescaled, resampled 3D radial images vs the multislice GRE acquisition for a COPD patient. For this subject, exhibiting a VDP of 35% on GRE, qualitative spatial agreement of the VDP regions between the resampled 3D radial and GRE maps is quite good. This is indicated by a relatively strong Dice coefficient of 0.7 for VDP in this subject. However, agreement for LVP is poor, with a Dice coefficient of 0.3. This may be

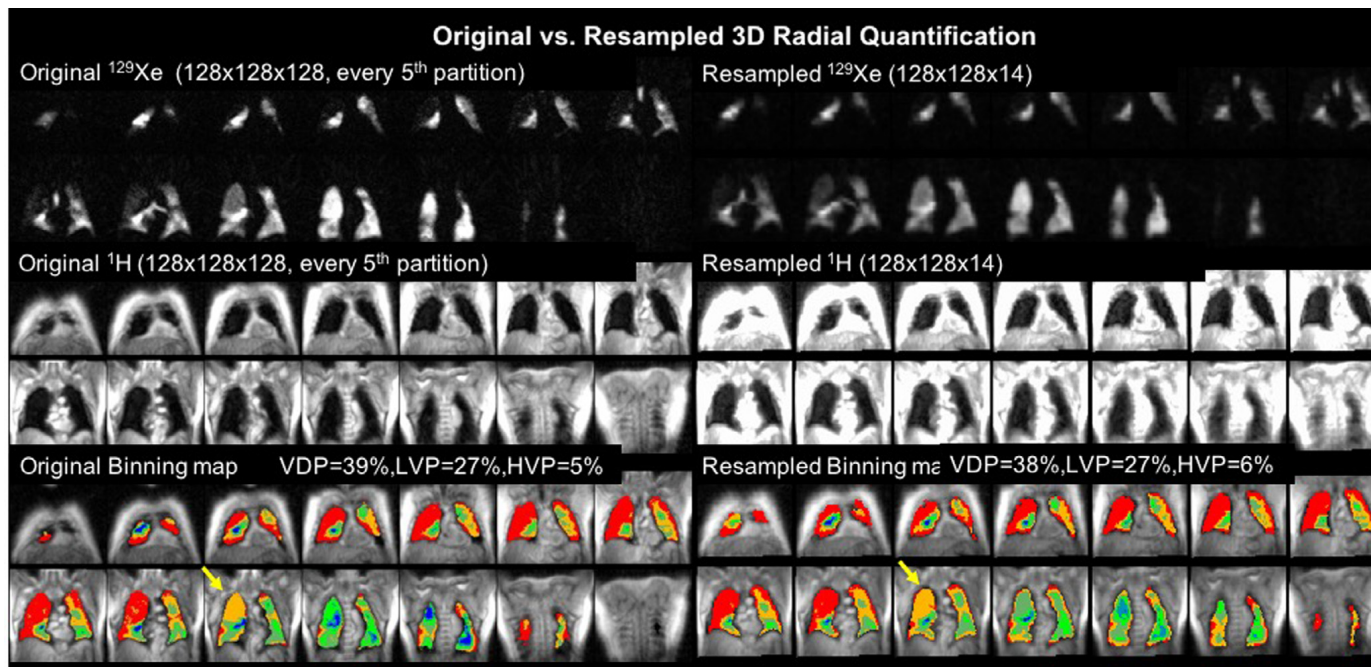


Figure 6. Representative ^{129}Xe ventilation MRI and maps for the original vs registered and down-sampled 3D radial images for a COPD patient (FEV1 = 66%). For the original vs resampled maps, VDP, LVP, and HVP were found to be 39% vs 38%, 27% vs 27%, and 5% vs 6%. After resampling, the defect and low-ventilation regions on the right upper lobe are preserved (arrows). COPD, chronic obstructive pulmonary disease; HVP, high-ventilation percentage; LVP, low-ventilation percentage; VDP, ventilation defect percentage.

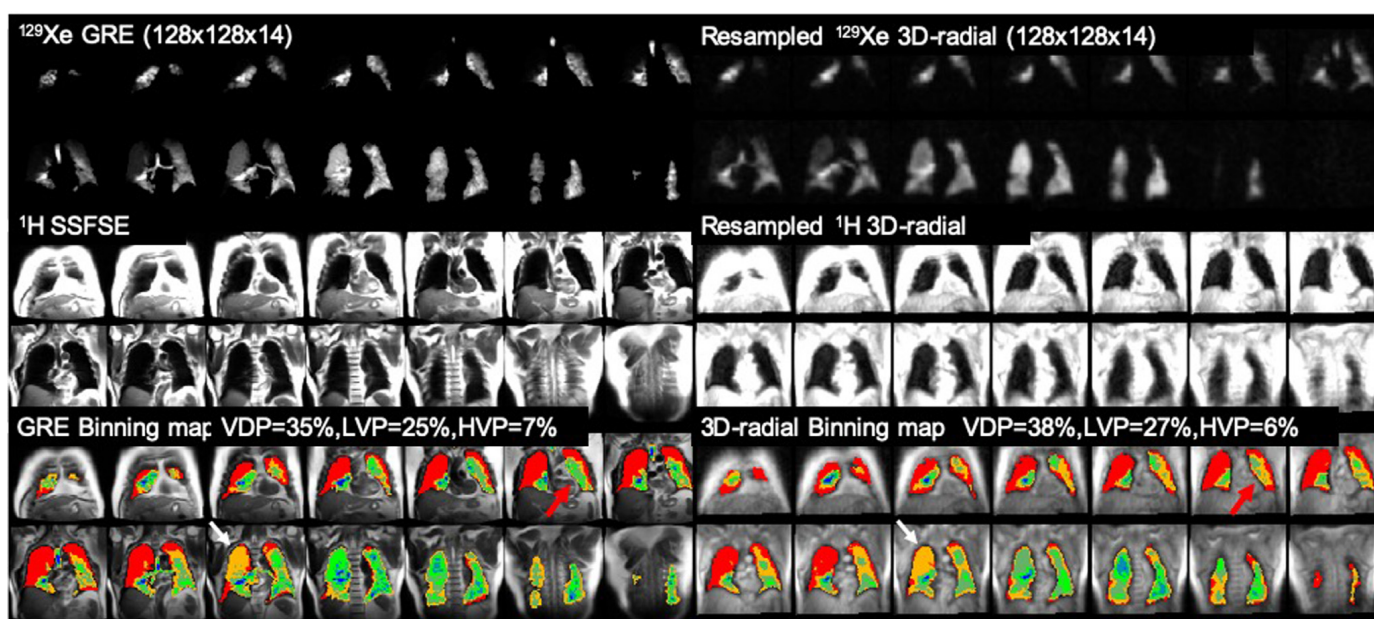


Figure 7. Comparison of the original multislice GRE ^{129}Xe ventilation MRI to the registered, down-sampled 3D radial images for the same patient COPD shown in [Figure 5](#). Although quantitative agreement for VDP, LVP, and HVP are excellent, the dice coefficients are moderate for VDP (0.7) and poor for LVP and HVP (0.3). COPD, chronic obstructive pulmonary disease; GRE, gradient recalled echo; HVP, high-ventilation percentage; LVP, low-ventilation percentage; VDP, ventilation defect percentage.

attributable to the regions in the anterior slices of the left upper lobe that appear normal on the GRE scan, but fall into the low ventilation bin on the resampled 3D radial images (arrows). Pixel-wise agreement was also relatively poor for HVP, although this is likely attributable to it encompassing a very small percentage of the lung in this patient. For the entire cohort, the spatial overlap between GRE and 3D radial was modest for VDP ($\text{Dice} = 0.5 \pm 0.2$), and relatively poor for LVP (0.3 ± 0.1) and HVP (0.2 ± 0.1). These results are summarized in [Table 2](#).

DISCUSSION

In order to evaluate the degree of agreement between quantitative metrics derived from 3D radial and multislice GRE ventilation images, it was necessary to establish a generalized means of determining quantitative binning thresholds. This is because the healthy reference distribution is not always a simple centered Gaussian as is serendipitously the case for commonly used coronal, multislice GRE imaging, acquired in

the anterior posterior direction. As the GRE sequence acquires images from anterior to posterior direction, the T1 effects obscure the natural anterior-posterior gradient. Specifically, the ventilation distribution derived from the 3D radial acquisition is skewed towards higher values, and is non-Gaussian in shape. However, analyzing images with such non-Gaussian distributions can be generalized by using a Box-Cox transformation to identify objective binning thresholds. Using this approach, the skewed or non-Gaussian healthy reference distributions is rendered into a normal distribution, from which a mean and SD can be derived to determine thresholds. The thresholds are then transformed back to the original histogram, and used to define the regions of VDP, LVP, MVP, and HVP. The resulting bins are no longer necessarily linearly spaced, but still encompass the same percentages of the reference distribution as the bins from a standard Gaussian distribution (34.1% for the bins within 1 SD of the mean, 13.6% for the next bin). Beyond solving the immediate image comparison problem in this work, this approach should enable the linear binning method

TABLE 2. Pixel-Wise Comparison of Quantitative Metrics Derived from GRE and Resampled 3D Radial

Statistic	COPD (n = 12)	LHF (n = 3)	PAH (n = 8)	CTEPH (n = 5)	NSIP (n = 13)	Total (n = 44)
<i>Dice coefficient</i>						
VDP	0.6 ± 0.1	0.5 ± 0.1	0.5 ± 0.1	0.3 ± 0.1	0.3 ± 0.1	0.5 ± 0.2
LVP	0.4 ± 0.1	0.3 ± 0.1	0.3 ± 0.0	0.3 ± 0.1	0.3 ± 0.1	0.3 ± 0.1
HVP	0.2 ± 0.1	0.2 ± 0.1	0.2 ± 0.0	0.2 ± 0.1	0.2 ± 0.1	0.2 ± 0.1

COPD, chronic obstructive pulmonary disease; CTEPH, chronic thromboembolic pulmonary hypertension; HVP, high-ventilation percentage; LHF, left heart failure; LVP, low-ventilation percentage; NSIP, nonspecific interstitial pneumonia; PAH, pulmonary artery hypertension; VDP, ventilation defect percentage.

to be easily applied to any acquisition that results in non-Gaussian healthy reference distributions. Note, that each different acquisition strategy will require its own reference distribution and Box-Cox transformation parameter of λ to derive appropriate thresholds.

Bland Altman analysis revealed relatively nonsignificant bias in comparing the VDP, LVP, and HVP derived from GRE vs radial scans ($\leq 2\%$). This suggests that the generalized approach to setting binning thresholds for 2D vs 3D scans is effective. Moreover, the limits of agreement were relatively good for VDP (-7% to 5%), reasonable for HVP (-8% to 8% , but somewhat broad for LVP (-10 to 14%). Although, these limits are encouraging, their magnitude is significantly higher than those reported in studies of repeat analysis, and comparisons between analysts, and centers. For context, the strictest limit can be taken from Santyr et al (8) who reported limits of agreement -0.84 to 1.03% for repeat analysis of VDP for the same scans of CF patients. Somewhat less stringent are the limits of agreement of -2.7% to 3% for VDP for different analysts from two different imaging centers analyzing the same scans using identical methods (23). This range is also comparable for VDP analyzed for the same datasets but using different methods (linear binning vs K-means), which yielded limits of agreement of (+%) (0.2% , 4%) (24). Further context can be gained from the previously reported analysis of two different GRE scans acquired in different breaths and at different resolutions, which yielded limits of -4% to 6% for VDP (18). Thus, while the field is still coming to an agreement on analysis methods, and focus is just now starting to turn to issues of repeatability and accuracy, a potentially reasonable target for limits of agreement on metrics derived from different or repeated acquisitions should be better than $\pm 5\%$.

There are several possible explanations for the somewhat broad limits of agreement observed in this work. These include obvious differences in acquisition strategy, resolution, histogram rescaling, bias field, and the fact that the scans were acquired during different breath-holds with slightly different volumes of xenon. Figure 8 shows four cases in which disagreement between the multislice GRE and 3D radial acquisitions was highest. Figure 8a shows a COPD patient with emphysematous bullae in the upper lobes, reflected as prominent LVP in the GRE scan, which is less evident on 3D radial and results in ΔLVP of 10% . The bullae may have a significant impact on respiratory mechanics (25) and in this case, likely resulted in different ventilation intensities between the breath-holds. Figure 8b shows a chronic thromboembolic pulmonary hypertension patient with moderately different distribution of VDP and a difference of 6% between the two acquisitions. In this patient the lung inflation level was quite different between scans ($\Delta TLV = 0.8$ L), which may have attributed to the different breath-holds. However, the scan with higher inflation exhibited higher VDP, which is opposite to what would be expected (26). It is noteworthy that total thoracic cavity volume was somewhat higher on GRE vs 3D radial scans (4.0 ± 1.2 L vs 3.7 ± 1.3 L), which may be

partially attributable to the greater slice thickness of GRE acquisition. Moreover, those images acquired with GRE underwent gradient wrap correction, whereas this was not done for the 3D radial scans that were reconstructed offline. It is also conceivable that patients could inhale the more diluted GRE xenon doses (250–500 mL) vs 700mL much easier than the denser 700 mL 3D radial doses. Another example is the COPD patient shown in Figure 8c in which VDP differed by 7% . In this subject many of the defects were small and patchy, and may have been better resolved in plane by the GRE acquisition. And finally, the COPD patient in Figure 8d shows ventilation defect regions that are significantly more contiguous in GRE vs radial, leading to a VDP that was 5% higher. This may be attributable to thicker slices leading to a more natural demarcation of the different clusters.

Three additional considerations that may have contributed to the broader limits of agreement for these scans include the effects of gravitational gradients (27), bias field correction and 3D radial reconstruction. Specifically, we know that 3D acquisitions will better preserve gravitational and other physiological-related intensity gradients because the entire volume is sampled throughout the breath-hold. By contrast, the multislice GRE sequence diminishes these gradients by virtue of its anterior-to-posterior slice acquisition (18). It is as yet unclear as to how effectively the bias field correction algorithm is able to distinguish true B1 inhomogeneity from physiological gradients. These algorithms, were originally developed for brain MRI (28) and although now routinely applied to lung MRI (28,29), it has not been specifically validated for functional imaging. Thus, it is conceivable that some image intensity gradients that are physiological in nature may inadvertently be “corrected” and contributed to widening the limits of agreement of the quantitative metrics. Moreover, the 3D radial scans are significantly undersampled with only 1000 radial spokes acquired. Although we have found 3D radial sequence has been insensitive to undersampling (20,30), it is worth noting that 3D radial image character does depend strongly on reconstruction parameters. These were optimized to generate optimal SNR and resolution for the ventilation images acquired within the constraints of the gas-exchange images. It will be necessary to conduct further rigorous studies to understand how different 3D radial reconstruction parameters influence the 3D radial image character and its quantification.

When comparing the maps on a pixel-by-pixel basis the level of agreement was modest for VDP, and relatively poor for the other ventilated clusters. Such comparisons are clearly the strictest possible test and are affected, not only by the factors already described, but by coregistration, interpolation, and down-sampling, which could particularly affect high-frequency information. Other important factors include the effects of lung volume, caused by different lung inflation levels between scans, differences in gradient wrap correction, or subtle intensity differences causing pixels moves from one intensity cluster to another. This comparison makes clear that

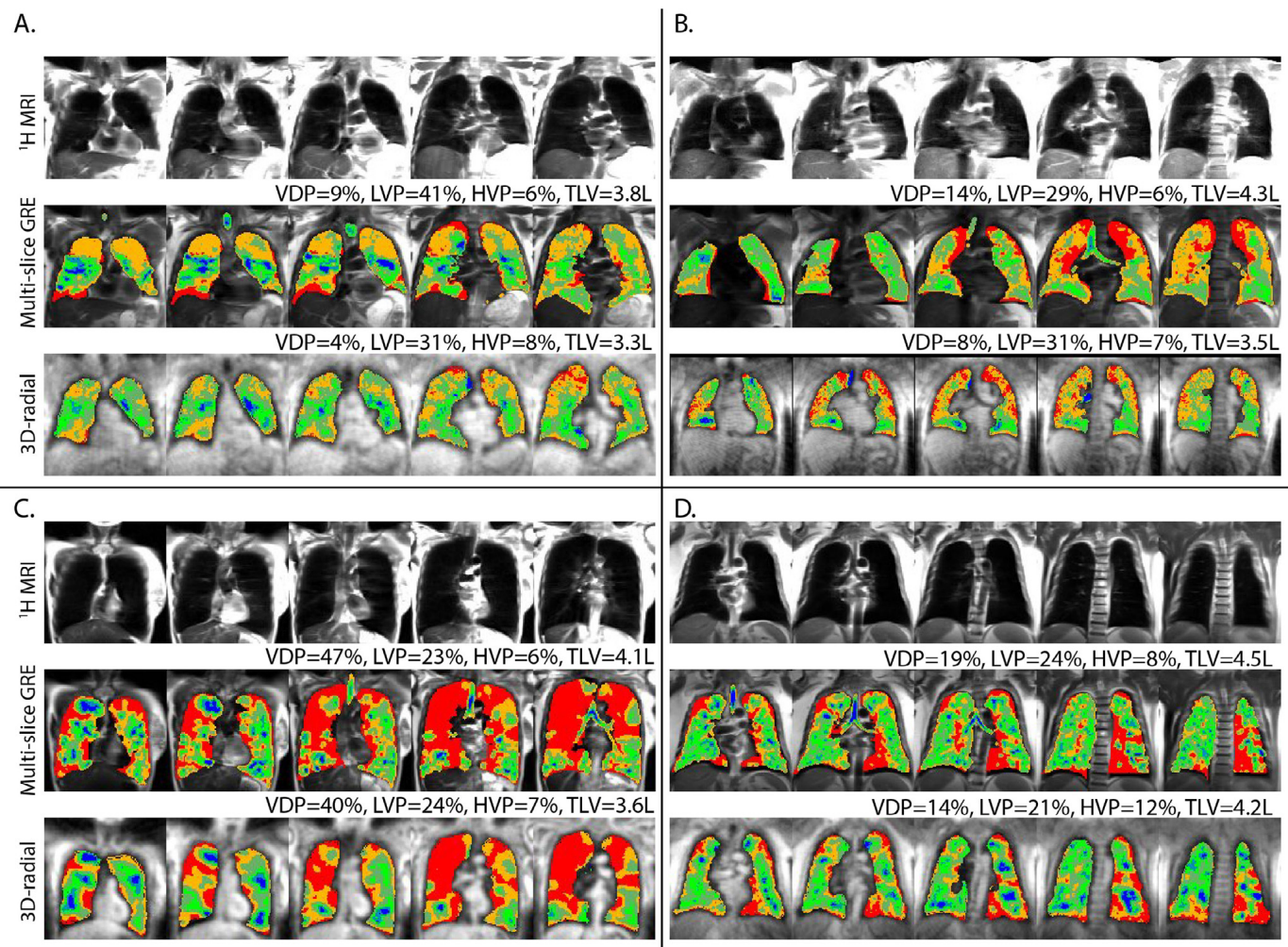


Figure 8. Representative outlier cases include (a) a COPD patient with emphysematous bullae, which likely caused differences in ventilation distribution between two scans. (b) a CTEPH patient with 0.8 liter inhalation difference between the multislice GRE scan and the 3D radial scan. (c) a COPD patient with numerous small and patchy ventilation defects throughout the lungs. (d) a COPD patient with patchy ventilation defects in the middle to posterior lungs. COPD, chronic obstructive pulmonary disease; HVP, high-ventilation percentage; LVP, low-ventilation percentage; TLV, total lung volume; VDP, ventilation defect percentage.

for applications such as monitoring therapeutic response or progression, we should use identical sequence for longitudinal scans.

In conclusion, both multislice GRE and 3D radial gas exchange MRI can image ventilation and produce qualitatively similar maps with quantitative metrics of VDP that agree relatively well. The multislice GRE acquisition provides high SNR and depicts ventilation features with greater in-plane detail. By contrast, 3D radial gas exchange MRI provides isotropic resolution and images both the ventilation and dissolved phase distributions. However, to achieve such dual phase imaging, the 3D radial image is undersampled and this may compromise the capability of resolving heterogeneously distributed defects. However, in cases where ventilation and/or changes to ventilation are not the primary focus, it is likely that combined 3D radial imaging will be sufficient. Nonetheless, for cases where subtle changes in ventilation (such as in asthmatic subjects pre- and post-bronchodilator) are of primary interest, a dedicated ventilation scan is likely still preferable.

ACKNOWLEDGMENTS

Funding: NIH/NHLBI-R01HL126771, R01HL105643.

REFERENCES

- Zha W, Kruger SJ, Cadman RV, et al. Regional heterogeneity of lobar ventilation in asthma using hyperpolarized helium-3 MRI. *Acad Radiol*. 2018; 25:169–178.
- He M, Driehuys B, Que L, et al. Using hyperpolarized ¹²⁹Xe MRI to quantify the pulmonary ventilation distribution. *Acad Radiol*. 2016; 23:1521–1531.
- Svenningsen S, Kirby M, Starr D, et al. Hyperpolarized He-3 and Xe-129 MRI: differences in asthma before bronchodilation. *J Magn Reson Imaging*. 2013; 38:1521–1530.
- Wang Z, Robertson SH, Wang J, et al. Quantitative analysis of hyperpolarized (¹²⁹)Xe gas transfer MRI. *Med Phys*. 2017; 44:2415–2428.
- Qing K, Ruppert K, Jiang Y, et al. Regional mapping of gas uptake by blood and tissue in the human lung using hyperpolarized xenon-129 MRI. *J Magn Reson Imaging*. 2014; 39:346–359.
- Kaushik SS, Freeman MS, Cleveland ZI, et al. Probing the regional distribution of pulmonary gas exchange through single-breath gas- and dissolved-phase ¹²⁹Xe MR imaging. *J Appl Physiol* (1985) 2013; 115:850–860.
- Virgincar RS, Cleveland ZI, Kaushik SS, et al. Quantitative analysis of hyperpolarized ¹²⁹Xe ventilation imaging in healthy volunteers and

- subjects with chronic obstructive pulmonary disease. *NMR Biomed.* 2013; 26:424–435.
8. Santyr G, Kanhere N, Morgado F, et al. Hyperpolarized gas magnetic resonance imaging of pediatric cystic fibrosis lung disease. *Acad Radiol.* 2019; 26:344–354.
 9. Rayment JH, Couch MJ, McDonald N, et al. Hyperpolarised (129)Xe MRI to monitor treatment response in children with cystic fibrosis. *Eur Respir J.* 2019.
 10. Kirby M, Pike D, Coxson HO, McCormack DG, Parraga G. Hyperpolarized He-3 ventilation defects used to predict pulmonary exacerbations in mild to moderate chronic obstructive pulmonary disease. *Radiology.* 2014; 273:887–896.
 11. Zha W, Niles DJ, Kruger SJ, et al. Semiautomated ventilation defect quantification in exercise-induced bronchoconstriction using hyperpolarized helium-3 magnetic resonance imaging: a repeatability study. *Acad Radiol.* 2016; 23:1104–1114.
 12. He M, Driehuys B, Que LG, et al. Using hyperpolarized 129Xe MRI to quantify the pulmonary ventilation distribution. *Acad Radiol.* 2016; 23:1521–1531.
 13. Doganay O, Matin TN, McIntyre A, et al. Fast dynamic ventilation MRI of hyperpolarized (129) Xe using spiral imaging. *Magn Reson Med.* 2018; 79:2597–2606.
 14. Stewart NJ, Norquay G, Griffiths PD, et al. Feasibility of human lung ventilation imaging using highly polarized naturally abundant xenon and optimized three-dimensional steady-state free precession. *Magnet Reson Med.* 2015; 74:346–352.
 15. Niedbalski PJ, Willmering MM, Robertson SH, et al. Mapping and correcting hyperpolarized magnetization decay with radial keyhole imaging. *Magn Reson Med.* 2019; 82:367–376.
 16. He M, Kaushik SS, Robertson SH, et al. Extending semiautomatic ventilation defect analysis for hyperpolarized Xe-129 ventilation MRI. *Acad Radiol.* 2014; 21:1530–1541.
 17. Driehuys B, Cates GD, Miron E, et al. High-volume production of laser-polarized Xe-129. *Appl Phys Lett.* 1996; 69:1668–1670.
 18. He M, Robertson SH, Kaushik SS, et al. Dose and pulse sequence considerations for hyperpolarized (129)Xe ventilation MRI. *Magn Reson Imaging.* 2015; 33:877–885.
 19. Wang Z, He M, Bier EA, et al. Hyperpolarized 129 Xe gas transfer MRI: the transition from 1.5T to 3T. *Magn Reson Med.* 2018; 80:2374–2383.
 20. Robertson SH, Virgincar RS, He M, et al. Optimizing 3D noncartesian gridding reconstruction for hyperpolarized 129Xe MRI—focus on pre-clinical applications. *Concepts Magn Reson Part A.* 2015; 44:190–202.
 21. Wang Z, He M, Bier E, et al. Hyperpolarized (129) Xe gas transfer MRI: the transition from 1.5T to 3T. *Magn Reson Med.* 2018; 80:2374–2383.
 22. Avants BB, Epstein CL, Grossman M, et al. Symmetric diffeomorphic image registration with cross-correlation: evaluating automated labeling of elderly and neurodegenerative brain. *Med Image Anal.* 2008; 12:26–41.
 23. Couch MJ, Thomen R, Kanhere N, et al. A two-center analysis of hyperpolarized 129Xe lung MRI in stable pediatric cystic fibrosis: potential as a biomarker for multi-site trials. *J Cyst Fibros.* 2019; 18:728–733.
 24. He M, Zha W, Tan F, et al. A comparison of two hyperpolarized 129Xe MRI ventilation quantification pipelines: the effect of signal to noise ratio. *Acad Radiol.* 2019; 26:949–959.
 25. Ruan S-Y, Huang C-T, Chien J-Y, et al. Non-surgical management of giant lung bullae during mechanical ventilation. *Respiratory care.* 2011; 56:1614–1616.
 26. Hughes PJC, Smith L, Chan HF, et al. Assessment of the influence of lung inflation state on the quantitative parameters derived from hyperpolarized gas lung ventilation MRI in healthy volunteers. *J Appl Physiol (1985)* 2019; 126:183–192.
 27. Prisk GK. The lung in space. *Clin Chest Med.* 2005; 26:415–438. vi.
 28. Tustison NJ, Avants BB, Cook PA, et al. N4ITK: improved N3 bias correction. *IEEE Trans Med Imaging.* 2010; 29:1310–1320.
 29. Tustison NJ, Avants BB, Flors L, et al. Ventilation-based segmentation of the lungs using hyperpolarized He-3 MRI. *J Magn Reson Imaging.* 2011; 34:831–841.
 30. Barger AV, Block WF, Toropov Y, et al. Time-resolved contrast-enhanced imaging with isotropic resolution and broad coverage using an undersampled 3D projection trajectory. *Magn Reson Med.* 2002; 48:297–305.